NACA RM L52G09

NACA

RESEARCH MEMORANDUM

PRELIMINARY INVESTIGATION OF THE LOW-AMPLITUDE DAMPING IN PITCH OF TAILLESS DELTA- AND SWEPT-WING CONFIGURATIONS AT MACH NUMBERS FROM 0.7 TO 1.35

By Charles T. D'Aiutolo and Robert N. Parker

Langley Aeronautical Laboratory
Langley Field, Va.

NATIONAL ADVISORY COMMITTEE
FOR AERONAUTICS

WASHINGTON

August 20, 1952
Declassified July 26, 1957

NATIONAL ADVISORY COMMITTEE FOR AERONAUTICS

RESEARCH MEMORANDUM

PRELIMINARY INVESTIGATION OF THE LOW-AMPLITUDE DAMPING IN PITCH OF TAILLESS DELTA- AND SWEPT-WING CONFIGURATIONS AT MACH NUMBERS FROM 0.7 TO 1.35

By Charles T. D'Aiutolo and Robert N. Parker

SUMMARY

A flight investigation was conducted using four rocket-propelled models of low-aspect-ratio tailless configurations between Mach numbers of 0.7 and 1.35. The configurations utilized in the investigation were a 45° delta-wing model with NACA 63A010 airfoil sections parallel to free stream, a 45° delta-wing model with NACA 63A006 airfoil sections parallel to free stream, a 37.5° swept-tapered-wing model with NACA 64_1A012 sections perpendicular to quarter chord, and a 39° swept-tapered-wing model with NACA 64A006 airfoil sections perpendicular to quarter chord. Information was obtained on the static and dynamic longitudinal stability and drag characteristics near zero lift by analyzing the free low-amplitude oscillations in pitch.

The results indicated that the damping in pitch was low at low amplitudes throughout the Mach number range investigated. At subsonic speeds the damping was stable; whereas at transonic speeds the damping was unstable. At low supersonic speeds the damping of the delta-wing models was unstable; whereas the damping of the swept-wing configurations was stable.

INTRODUCTION

The aerodynamic problems associated with high-speed flight have caused radical departures in aircraft design. Many aircraft configurations have been proposed and one of these is the low-aspect-ratio tailless configuration. One disadvantage of this type of configuration, however, is that, at transonic and low supersonic speeds, the dynamic

longitudinal stability is low. In order to provide basic experimental data on this phenomenon, the Pilotless Aircraft Research Division has begun a flight investigation to determine the dynamic longitudinal stability characteristics of low-aspect-ratio tailless configurations. The present paper contains the first results from the flight tests of four rocket-propelled models of this investigation; a 45° delta-wing configuration incorporating NACA 63A010 airfoil sections, a 45° delta-wing configuration incorporating 63A006 airfoil sections, a 37.5° swept-tapered wing configuration incorporating NACA 64_1A012 airfoil sections, and a 39° swept-tapered wing configuration incorporating NACA 64A006 sections. The data are presented over a Mach number range of 0.7 to 1.35 corresponding to a Reynolds number range of 5.2×10^6 to 14.3×10^6, respectively.

The static and dynamic longitudinal stability characteristics were determined by analyzing the free oscillations of the models as they traversed the speed range and the drag characteristics were determined from the deceleration of the models. The models were flown at the Langley Pilotless Aircraft Research Station at Wallops Island, Va.

SYMBOLS

a_n	reading of normal accelerometer, g
V	velocity of flight, ft/sec
M	Mach number, $\frac{V}{\text{Speed of sound}}$
R	Reynolds number (based on respective mean aerodynamic chords of models)
$\bar{c}$	mean aerodynamic chord, ft
S	total wing area, sq ft
P	period of short-period oscillation, sec
q	dynamic pressure, lb/sq ft
b	total damping factor
$T_{1/2}$	time required for short-period oscillation to damp to one-half amplitude, sec

T_2 time required for short-period oscillation to double in amplitude, sec

k reduced frequency parameter (based on respective mean aerodynamic chord of models), $\frac{\omega \bar{c}}{2V}$

I_y moment of inertia in pitch, slug-ft^2

C_{m_α} static stability derivative

$C_{m_q} = \frac{\partial C_m}{\partial \frac{\dot{\theta} \bar{c}}{2V}}$, per radian

$C_{m_{\dot{\alpha}}} = \frac{\partial C_m}{\partial \frac{\dot{\alpha} \bar{c}}{2V}}$, per radian

C_{L_α} slope of the lift curve

$C_{D_{C_{L \approx 0}}}$ drag coefficient near zero lift (based on total included wing areas)

$C_{L_{trim}}$ trim lift coefficient

α angle of attack of body, deg

α_{trim} trim angle of attack, deg

$\dot{\alpha} = \frac{1}{57.3} \frac{d\alpha}{dt}$, radian/sec

θ angle of pitch, radians

$\dot{\theta} = \frac{d\theta}{dt}$, radians/sec

ω frequency of short-period oscillation, radians/sec

MODELS AND APPARATUS

The general arrangements of the models are shown in figure 1, and the geometric characteristics of the models are presented in table I. Photographs of the models are shown in figure 2, and a photograph of a typical model-booster combination is shown in figure 3. Each model consisted of a basic fuselage to which was attached the wing under test. The fuselage was a body of revolution of fineness ratio 10, consisting of an ogival nose section and a cylindrical body section. Construction of the fuselage was principally of duralumin with magnesium skin. The nose section contained the telemeter; the cylindrical body section contained the wing mount and necessary fairings, the sustainer rocket motor, and the vertical tails.

The wings of the models were constructed principally of wood with sheet aluminum inlays. The vertical tails were constructed of duralumin.

All models contained a four-channel telemeter; measurements were made of the normal and longitudinal accelerations, angle of attack, and total pressure. The angle of attack was measured by a vane-type instrument located on a sting forward of the nose of the models (ref. 1), and the total-pressure tube was located on a strut below the fuselage of the models.

Additional velocity data were obtained by CW Doppler radar set; range and elevation of the models during flight, by tracking radar; atmospheric conditions, by a radiosonde; the first portion of the flights was recorded by special cameras.

Each model contained a cordite sustainer rocket motor and was boosted by a light-weight 5-inch HVAR rocket motor. Upon burnout of the booster rocket motor, the model separated from the booster, and the sustainer rocket motor was fired so that the model was propelled to the maximum speed. Upon burnout of the sustainer motor, the model coasted through the test speed range.

All booster-model combinations were launched from a rail-type launcher as shown in figure 3.

Test Technique

The models were allowed to fly freely throughout the test speed range and were not forcibly disturbed in pitch. The models experienced free oscillations from about $M = 0.83$ to about $M = 1.35$; at Mach numbers less than $M = 0.83$ these free oscillations were not apparent.

The desired static and dynamic longitudinal stability derivatives were obtained, wherever possible, from these oscillations. In all cases, the trace of the normal accelerometer was used to reduce the data. For each oscillation used, the dynamic pressure q was considered constant during that oscillation, since the error caused by a change in q was negligible. Roll data, not presented, indicated that for all models the rate of roll was approximately zero.

The scale of the tests is presented in figure 4 by a plot of Reynolds number against Mach number for each of the four models; the Reynolds number is based on the respective mean aerodynamic chords. Figure 5 is a plot of the variation of dynamic pressure against Mach number.

RESULTS AND DISCUSSION

The method of reducing the data and the accuracy of the results presented herein are described in detail in appendix A of reference 2. A discussion of the method of obtaining the total damping factor is included in this paper under the section entitled "Dynamic Longitudinal Stability."

All of the stability parameters presented in this paper were determined from the coasting phase of the flights and are for a center-of-gravity position of 17 percent of the mean aerodynamic chord behind the leading edge of the mean aerodynamic chord.

Time History

A typical reduced time history of the motions encountered during the flights is presented in figure 6 where the trace of the normal accelerometer and the Mach number are shown as a function of the flight time over which the free oscillations were experienced. It is believed that these free oscillations are associated with low angles of attack and would not occur at moderate or high angles of attack. The amplitudes of the free oscillations as recorded by the normal accelerometer were small (maximum variation is of the order of $\pm 1.0g$) and correspond to an angle-of-attack range of $\pm 0.5^{\circ}$.

It may be seen from figure 6 that model 3 (swept thick-wing-configuration) experienced a longitudinal trim change between flight time of 7.3 seconds and 10.9 seconds, corresponding to $M = 1.00$ and $M = 0.80$, respectively. This trim change was about 0.22 trim lift coefficient and corresponded to a nose-down change in trim angle of attack of about 0.2°. Model 3 also experienced a low-lift buffet, not shown, between flight times of 7.3 seconds and 7.7 seconds corresponding to $M = 1.00$ and $M = 0.94$, respectively, the frequency of which was about 135 cycles per second.

Models 1, 2, and 4 did not experience either a longitudinal trim change or a low-lift buffet.

Static Longitudinal Stability

The static longitudinal stability characteristics, the periods of the free oscillations, and the static-stability derivative are presented in figure 7 for each of the models.

The periods of the random oscillations are presented in figure 7(a) where it can be seen that there is considerable scatter in the data for each of the models. It was possible, however, to fair curves through the test data points and the faired curves indicate a decrease in period with an increase in Mach number. This variation of the period with Mach number compares favorably with other rocket-powered models of like mass and flight characteristics.

The static stability derivative, C_{m_α}, for each of the models is presented in figure 7(b) where the values obtained are based on a system with a single degree of freedom (because of the low-amplitude angle-of-attack variation) and were calculated by the use of the following expression

$$C_{m_\alpha} = -0.688 \frac{I_y}{P^2 qs\bar{c}}$$

where the values of P were determined from the faired curves of the periods of the random oscillations against Mach number.

The static stability derivative of each of the models increased rapidly with increasing Mach number through the transonic speed region and then decreased somewhat as the Mach number became greater than one.

Dynamic Longitudinal Stability

The equation for the free oscillations of a system with two degrees of freedom is as follows:

$$\frac{a_n}{g} = \left(\frac{a_n}{g}\right)_{trim} + Ke^{+bt}(\sin \omega t + \varphi)$$

where $\left(\frac{a_n}{g}\right)_{trim}$ is the mean value about which the normal acceleration oscillates, K is a constant, and b is the total damping factor.

This total damping factor may be determined from the envelope curves enclosing the oscillations as

$$b = \frac{\log_e \frac{\Delta a_{n_2}}{\Delta a_{n_1}}}{t_2 - t_1}$$

where $t_2 - t_1$ is the period of the oscillations. This total damping factor is the true damping of the system and includes the contributions of the moment due to motion along a curved path at constant angle of attack C_{m_q}; the moment due to plunging motion with constant vertical acceleration $C_{m_{\dot{\alpha}}}$; and the slope of the lift-curve (see appendix A of ref. 1).

From the time histories of the motions encountered during the flights of the models, the total damping factor was obtained. Figure 6 is a typical time history of motion on which envelopes have been drawn and trim values determined for each of the oscillations used to determine values of this total damping factor.

The dynamic-longitudinal-stability parameters, the total damping factor, and the time to damp to both one-half amplitude and double amplitude are presented in figure 8 for each of the four models.

The variation of the total damping factor b with Mach number is presented in figure 8(a). Each model shows an abrupt decrease in the total damping factor from positive (stable) to negative (unstable) values for relatively small increments of Mach number at high subsonic speeds. As the Mach number increases, the total damping increases, becomes stable for the swept-wing configurations, but remains in the unstable region to the limit of the Mach number tested for the delta-wing configurations.

It may also be seen that the delta-wing configurations (models 1 and 2) became dynamically unstable at a lower Mach number than the swept-wing configurations (models 3 and 4). The delta-wing configurations remained unstable over wider limits of Mach numbers than did the swept-wing configurations. When models 1 and 2, thick-delta-wing configuration and thin-delta-wing configuration, respectively, are compared, it may be seen that model 1 (thick wing) became unstable at a lower Mach number than model 2 (thin wing) and both models remained unstable to the limit of Mach number tested. Both models, however, had about the same amount of dynamic instability. When models 3 and 4, thick-swept-wing configuration and thin-swept-wing configuration, respectively, are compared, model 3 (thick wing) had better total damping characteristics than model 4 (thin wing) and the region of dynamic instability for model 3 was smaller

than model 4. Of the four models tested, model 3 (thick-swept configuration) experienced the least amount of dynamic instability throughout the Mach number range investigated.

Although these free oscillations showed that all the models had low dynamic stability, the motions were not violent and the models traversed the speed range with no adverse effects. In the event that an artificial damper, which would be used to damp these oscillations, were to become inoperative, the results would not be catastrophic.

From the total damping factor b the time to damp to one-half amplitude $T_{1/2}$ and the time to double amplitude T_2 is obtained. These data are presented in figure 8(b) where it can be seen that, for each of the four models, both $T_{1/2}$ and T_2 indicate that the motions of the models converge rapidly when stable and diverge rapidly when unstable. It may be seen that the damping is more sensitive to changes in Mach number at transonic speeds than at supersonic speed.

When figures 7 and 8 are compared, it may be seen that each model was statically stable throughout the Mach number range investigated but dynamically unstable, to various degrees, in the transonic speed region.

Order of Oscillation Frequency

The random oscillations of the motions encountered during the flights of the models were analyzed further in order to determine whether unsteady flow effects, namely, the effects of higher order frequency terms, should be accounted for in the reduction of the data.

From the faired curves of the periods of the short-period oscillations of each model, the reduced frequency parameter $k = \frac{\omega \bar{c}}{2V}$ (based on respective mean aerodynamic chords) was determined and the maximum value obtained was $k = 0.0245$. Because the maximum value of k was small, it is believed that the effects of unsteady flows are not required in the determination of the damping-in-pitch derivatives in the present cases.

Rotational Damping in Pitch

The total damping factor b as obtained for models 2, 3, and 4 was reduced to determine the rotational damping-in-pitch derivatives $C_{m_q} + C_{m_{\dot{\alpha}}}$ for these models. Since values of the slope of the lift curve C_{L_α} could not be determined accurately in these tests because of low

angles of attack, the derivatives $C_{m_q} + C_{m_{\dot{\alpha}}}$ were determined from the total damping factor b by applying experimentally determined values of C_{L_α} obtained in other tests. The variation of C_{L_α} with Mach number for model 2 was obtained from reference 3 and for model 3 from reference 4. The variation of C_{L_α} with Mach number for model 4 was obtained from reference 5 to $M = 1.18$. At higher Mach numbers, the value C_{L_α} was extrapolated.

A comparison of the variation of $C_{m_q} + C_{m_{\dot{\alpha}}}$ with Mach number of the data reported herein (models 2, 3, and 4), the data as obtained from reference 6, the theory of reference 7 (center of gravity at 17 percent mean aerodynamic chord), the data of reference 8, and the data of reference 9 are presented in figure 9. The correlation of the data reported herein, model 2 (thin-delta-wing configuration), with other tests is fair. The regions of instability $\left(C_{m_q} + C_{m_{\dot{\alpha}}} \text{ positive}\right)$, however, are believed to be in good agreement when it is considered that the tests were conducted at two different center-of-gravity positions. These results are substantiated by the analysis presented in reference 6 where a theoretical stability boundary, based on two degrees of freedom, was calculated as a function of center-of-gravity position. A delta-wing configuration with center-of-gravity position at 17 percent mean aerodynamic chord will experience instability over wider limits of Mach number than one with center-of-gravity position at 35 percent mean aerodynamic chord. The supersonic theory (center of gravity at 17 percent mean aerodynamic chord) and the data of model 2 show agreement near $M = 1.3$.

The correlation of the data of model 3 (thick-swept-wing configuration) with the results of reference 8 is good. Both the subsonic test results (ref. 8) and the data of model 3 indicate positive (unstable) values of $C_{m_q} + C_{m_{\dot{\alpha}}}$ above a Mach number of 0.92. The data of model 3 indicate that the region of instability is narrow, about $M = 0.92$ to $M = 0.98$.

The correlation of data of model 4 (thin-swept-wing configuration) with the tests of reference 9 is fair; the reference tests indicate a lower Mach number for instability $M = 0.85$ than the results of model 4 $M = 0.93$. Possible reasons for this variation are that the configuration of reference 9 contained blunt trailing edges in the dive-brake region; whereas model 4 did not contain any such device. The geometric characteristics of the two configurations were also somewhat different.

DRAG

The drag coefficient near zero lift $C_{D_{C_{L\approx 0}}}$ based on total wing area is shown in figure 10 for all models. Models 1 and 3 (thick-wing configurations) experience the drag rise at lower Mach numbers and have higher supersonic drag than models 2 and 4 (thin-wing configurations).

CONCLUDING REMARKS

From the results of the flight tests of the four tailless models of low-aspect-ratio configurations, a 45° delta-wing configuration incorporating NACA 63A010 airfoil sections, a 45° delta-wing configuration incorporating NACA 63A006 airfoil sections, a 37.5° swept-tapered-wing configuration incorporating NACA 64_1A012 airfoil sections, and a 39° swept-tapered-wing configuration incorporating NACA 64A006 airfoil sections, the following concluding remarks may be stated: All models experienced low-amplitude free oscillations throughout the speed range investigated; the models were statically stable throughout the Mach number range investigated but were dynamically unstable, to various degrees, at transonic speeds for low amplitudes.

Langley Aeronautical Laboratory
National Advisory Committee for Aeronautics
Langley Field, Va.

REFERENCES

1. Mitchell, Jesse L., and Peck, Robert F.: An NACA Vane-Type Angle-of-Attack Indicator for Use at Subsonic and Supersonic Speeds. NACA RM L9F28a, 1949.

2. Gillis, Clarence L., Peck, Robert F., and Vitale, A. James: Preliminary Results From a Free-Flight Investigation at Transonic and Supersonic Speeds of the Longitudinal Stability and Control Characteristics of an Airplane Configuration With a Thin Straight Wing of Aspect Ratio 3. NACA RM L9K25a, 1950.

3. Sleeman, William C., Jr., and Becht, Robert E.: Aerodynamic Characteristics of a Delta Wing With Leading Edge Sweptback 45°, Aspect Ratio 4, and NACA 65A006 Airfoil Section. Transonic-Bump Method. NACA RM L9G22a, 1949.

4. Litchfield, A. F.: Summary of High Speed Aerodynamic Model Test Data for XF7U-1 Airplane. Rep. No. 7372, Chance Vought Aircraft, Div. of United Aircraft Corp. (Stratford, Conn.) Apr. 1, 1948.

5. Sleeman, William C., Jr., and Becht, Robert E.: Aerodynamic Characteristics of a Wing With Quarter-Chord Line Swept Back 35°, Aspect Ratio 4, Taper Ratio 0.6, and NACA 65A006 Airfoil Section. Transonic-Bump Method. NACA RM L9B25, 1949.

6. Tobak, Murray, Reese, David E., Jr., and Beam, Benjamin H.: Experimental Damping in Pitch of 45° Triangular Wings. NACA RM A50J26, 1950.

7. Henderson, Arthur, Jr.: Pitching-Moment Derivatives C_{m_q} and $C_{m_{\dot{\alpha}}}$ at Supersonic Speeds for a Slender-Delta-Wing and Slender-Body Combination and Approximate Solutions for Broad-Delta-Wing and Slender-Body Combinations. NACA TN 2553, 1951.

8. Mitchell, Jesse L.: The Static and Dynamic Longitudinal Stability Characteristics of Some Supersonic Aircraft Configurations. NACA RM L52A10a, 1952.

9. Sadoff, Melvin, Ankenbruck, Herman O., and O'Hare, William: Stability and Control Measurements Obtained During USAF-NACA Cooperative Flight-Test Program on the X-4 Airplane (USAF No. 46-677). NACA RM A51H09, 1951.

TABLE I.- GEOMETRIC CHARACTERISTICS OF THE MODELS

	Model 1	Model 2	Model 3	Model 4
Wing:	Delta	Delta	Swept	Swept
Total area, sq ft	5.00	5.00	4.96	3.72
Span, ft	4.47	4.47	3.86	3.65
Aspect ratio	4.0	4.0	3.0	3.6
Mean aerodynamic chord, ft	1.49	1.49	1.31	1.04
Sweepback of leading edge, deg	45.0	45.0	37.5	39.0
Dihedral, deg	0	0	0	0
Taper ratio	0	0	0.6	0.4
Airfoil sections	NACA 63A010, free stream	NACA 63A006, free stream	NACA 64_1A012, perpendicular to c/4	NACA 64A006, perpendicular to c/4
Fuselage:				
Fineness ratio	10	10	10	10
Miscellaneous:				
Model weight, lb	106	103	112	101
Moment of inertia in pitch, I_y, slug-ft^2	10.55	10.62	10.38	9.26
Center-of-gravity position, percent of M.A.C. (percent $\bar{c}$)	17	17	17	17
Wing loading, lb/sq ft	21.2	20.6	22.6	27.6

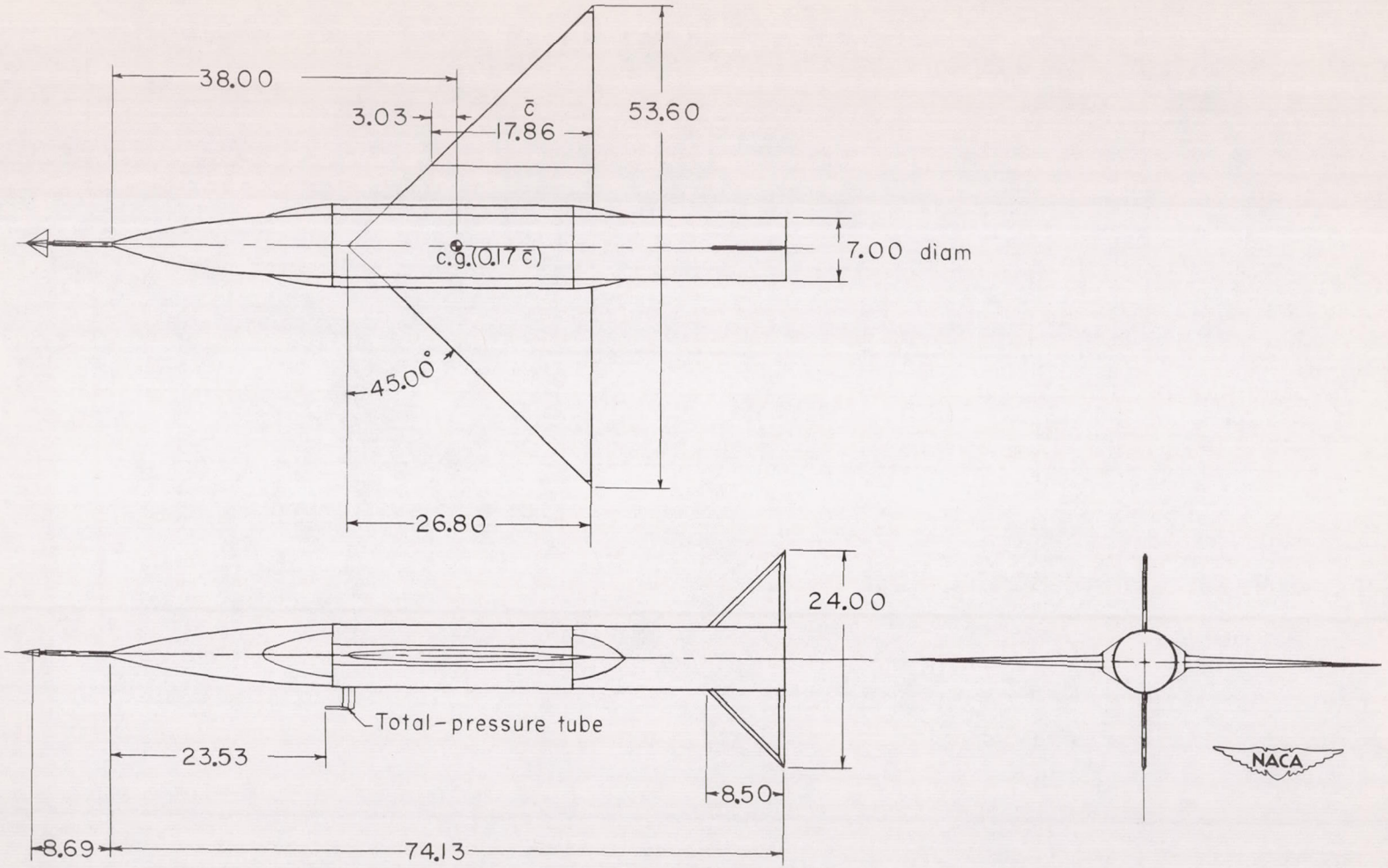

(a) Delta-wing configurations. Models 1 and 2.

Figure 1.- General arrangement of models. All dimensions are in inches unless noted.

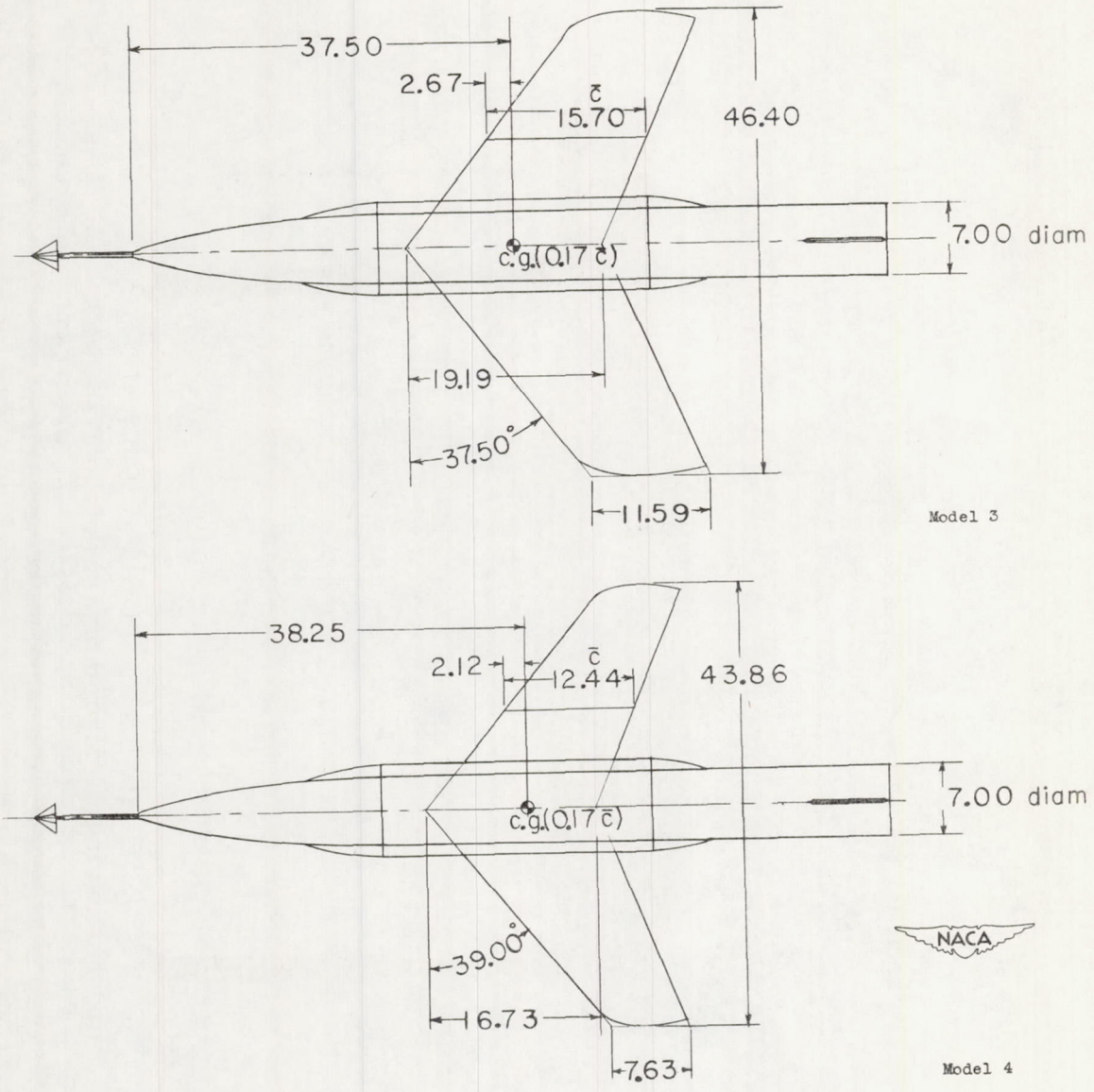

(b) Swept-wing configurations.

Figure 1.- Concluded.

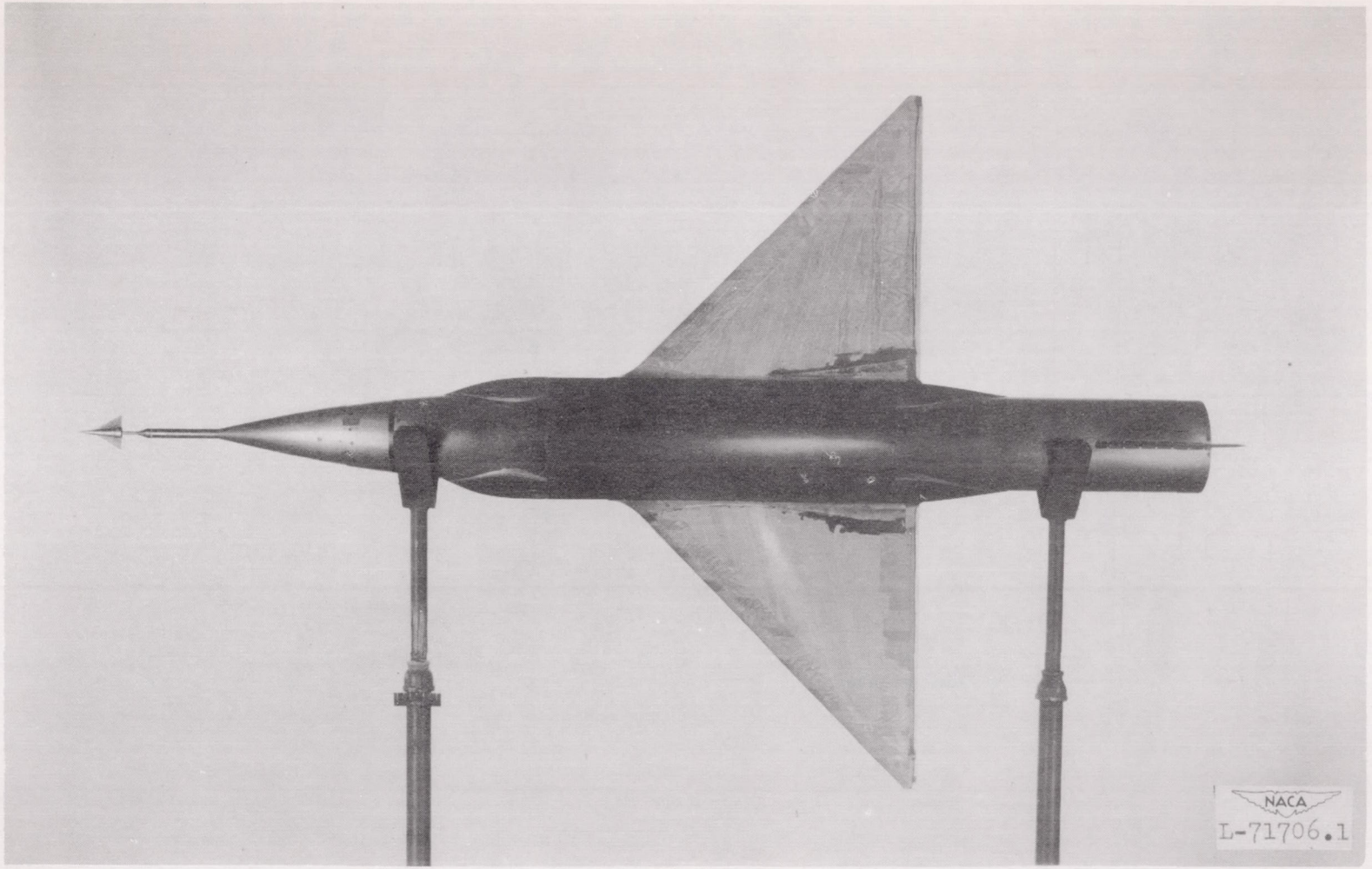

(a) Delta-wing configurations. Models 1 and 2.

Figure 2.- Photographs of models.

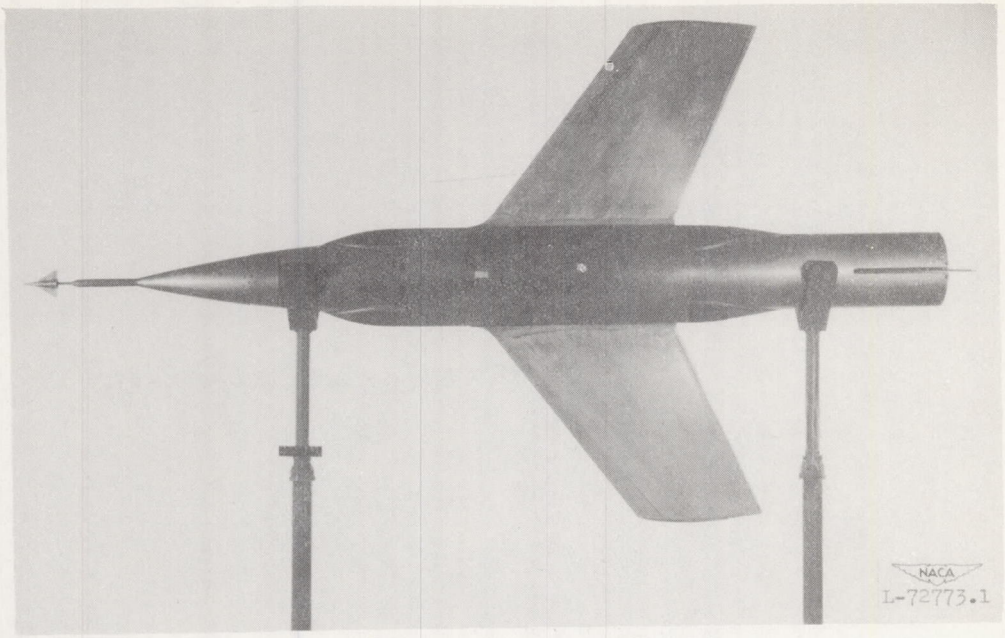

Model 3

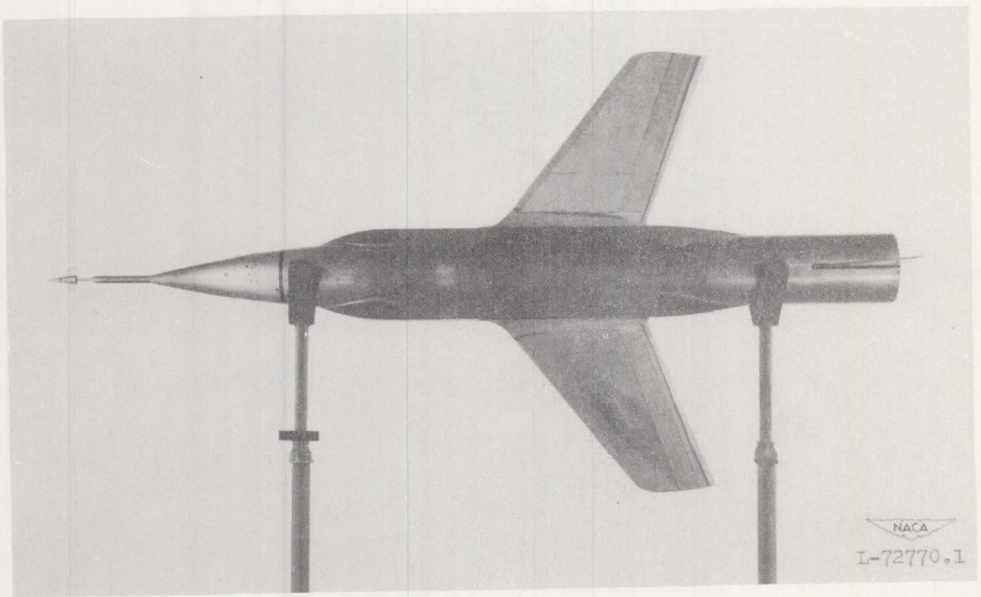

Model 4

(b) Swept-wing configurations.

Figure 2.- Concluded.

Figure 3.- Launching of a typical model-booster combination.

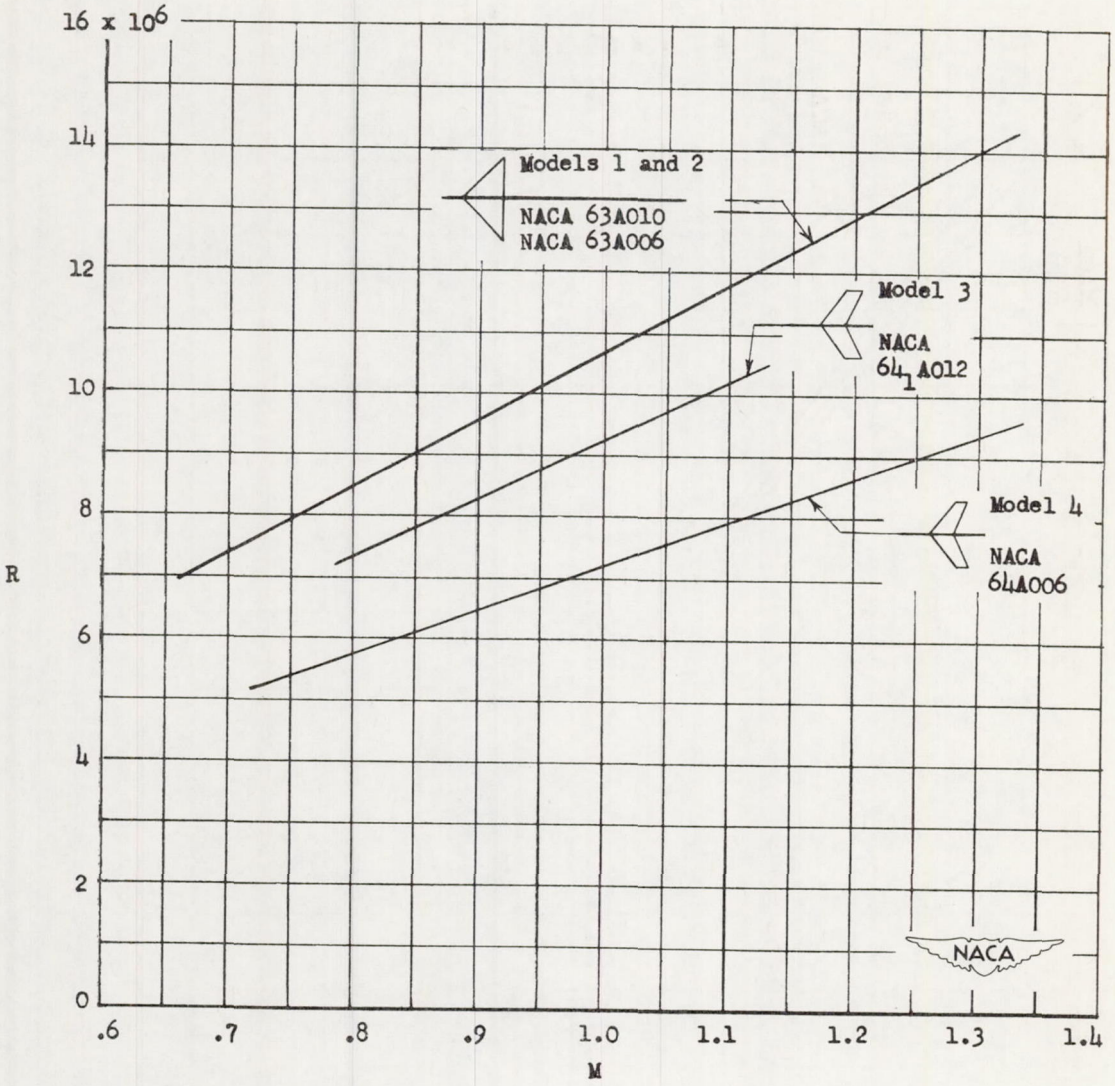

Figure 4.- Scale of tests based on respective mean aerodynamic chords.

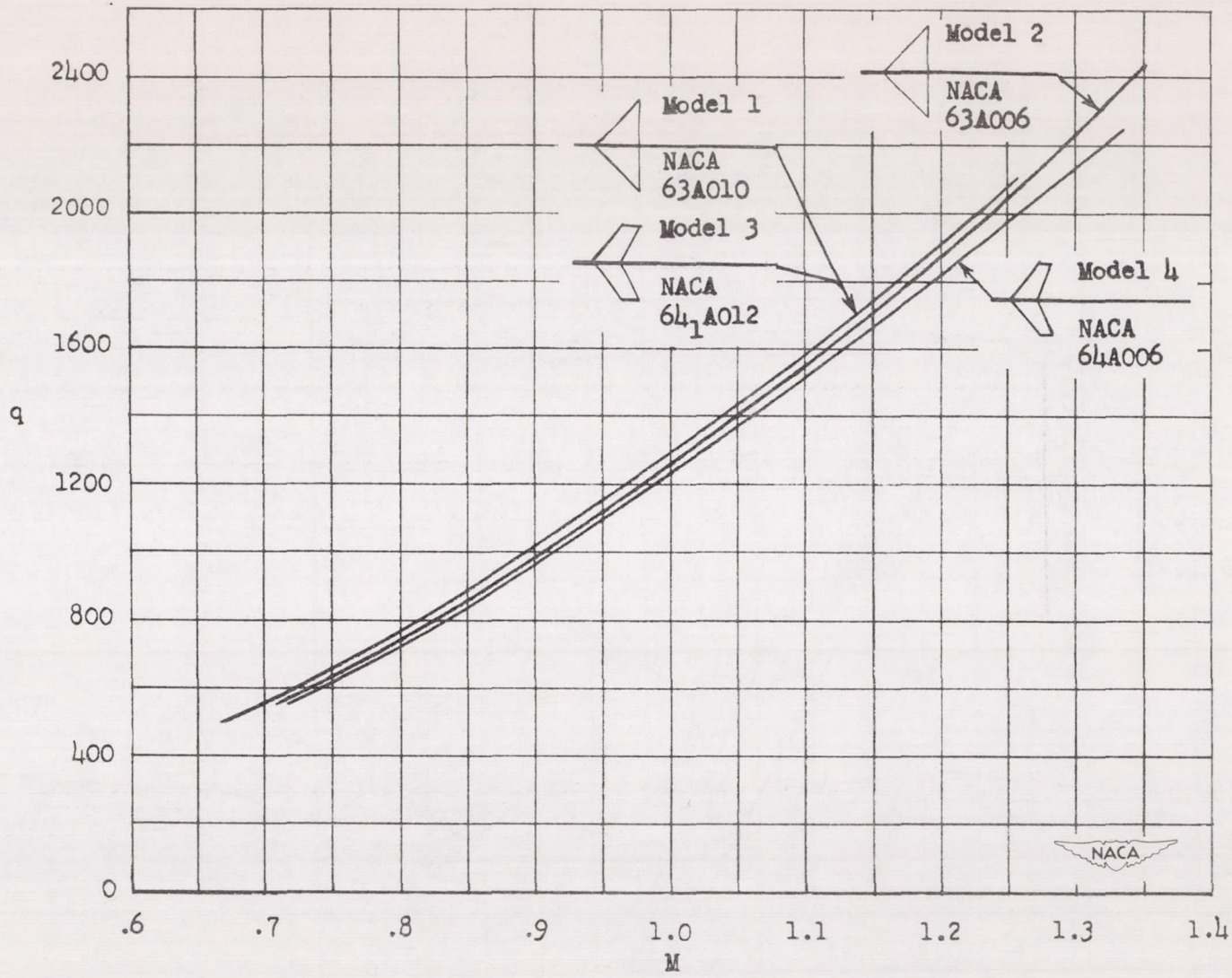

Figure 5.- Variation of dynamic pressure with Mach number.

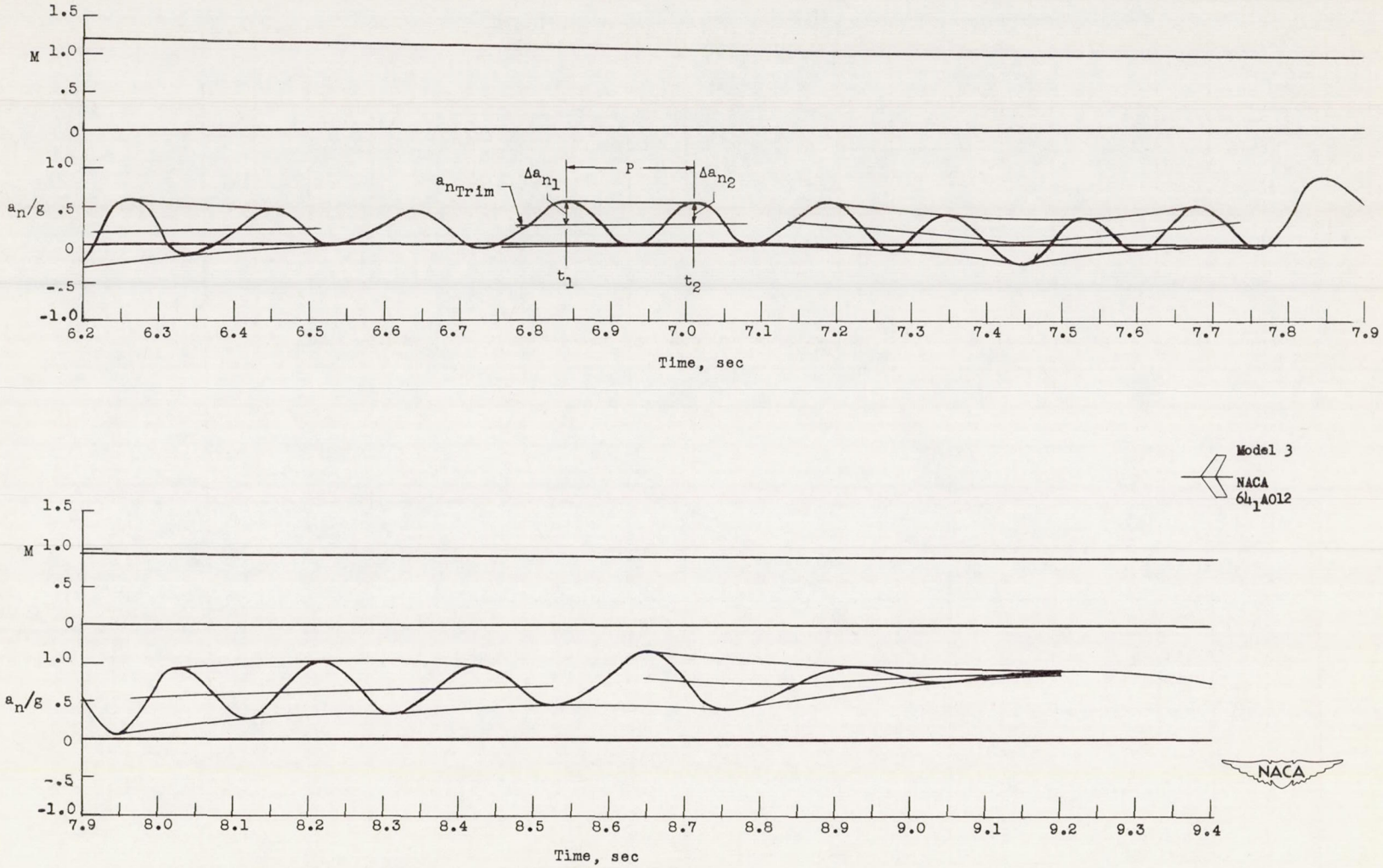

Figure 6.- Typical variation of normal accelerometer reading and Mach number with time.

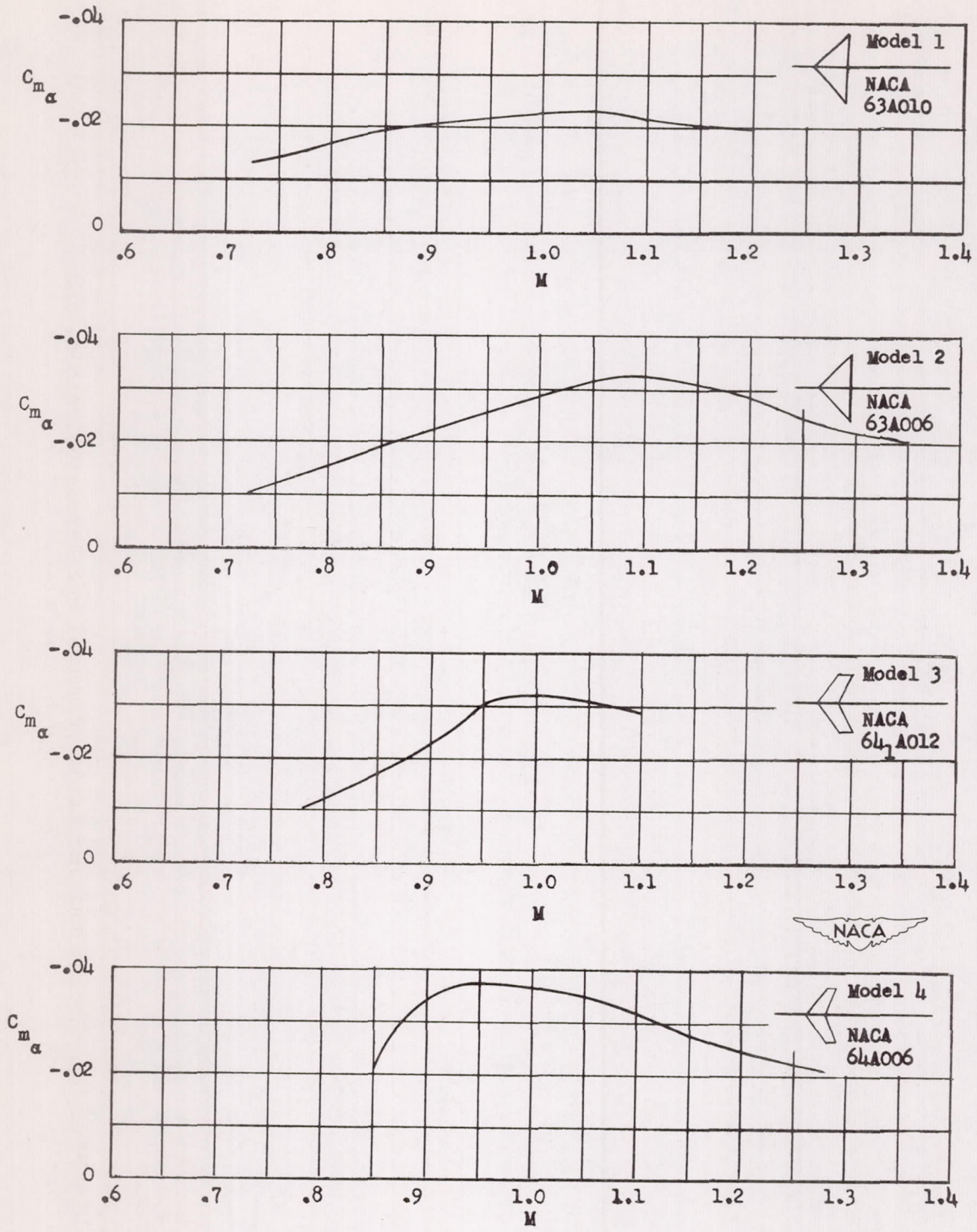

(b) Slope of pitching-moment curve.

Figure 7.- Concluded.

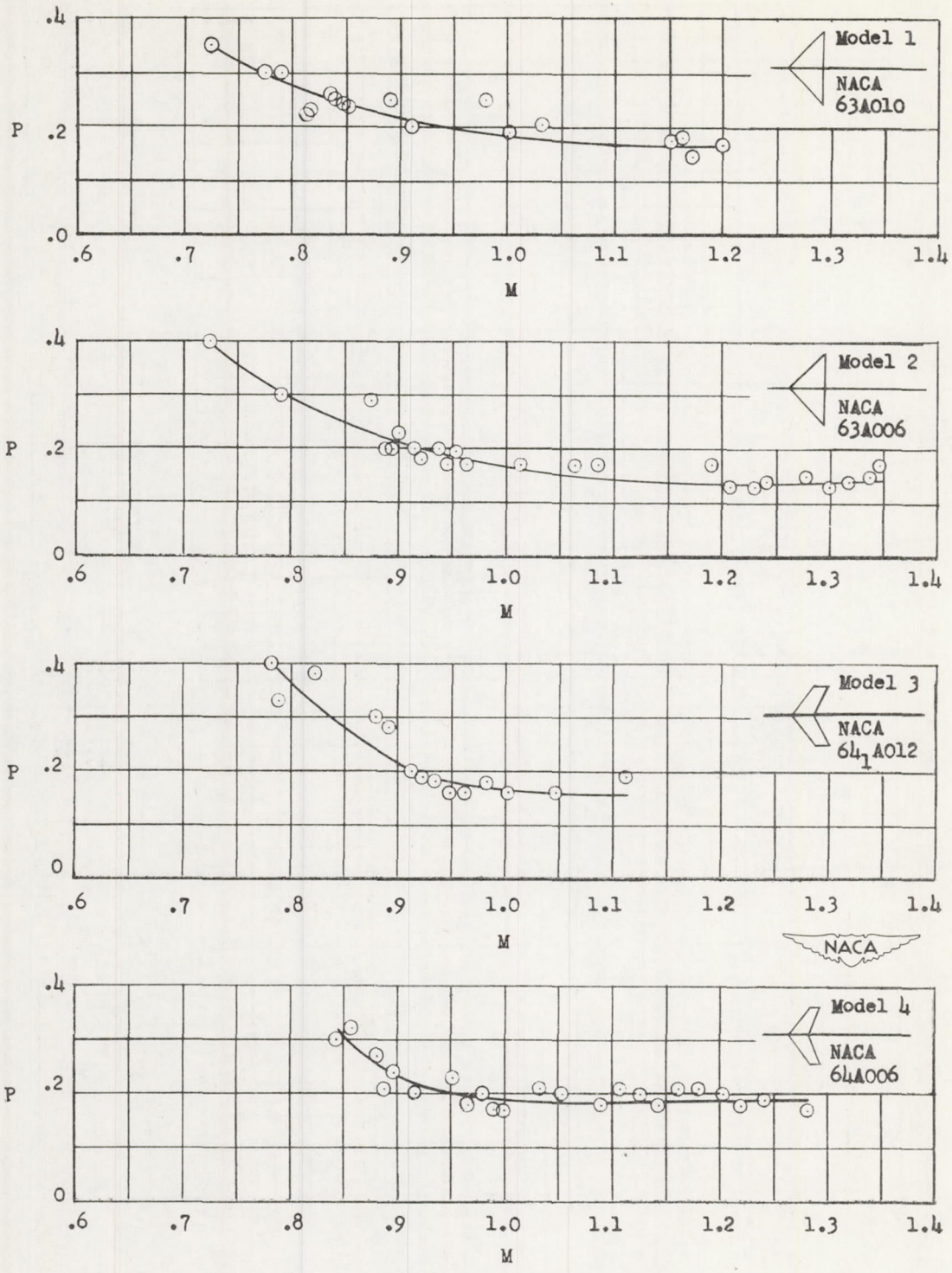

(a) Periods of oscillations.

Figure 7.- Variation of the static stability characteristics with Mach number.

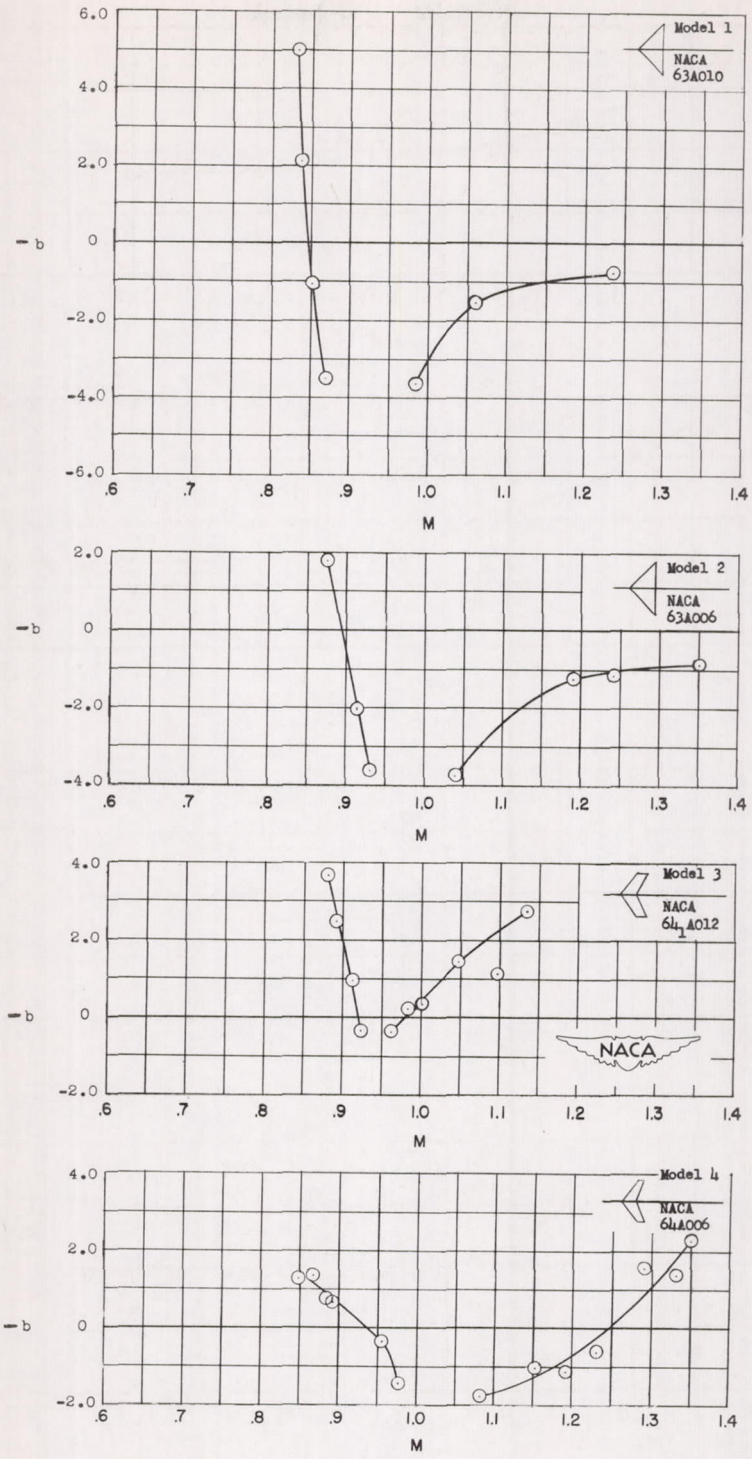

(a) Total damping factor.

Figure 8.- Variation of the dynamic stability characteristics with Mach number.

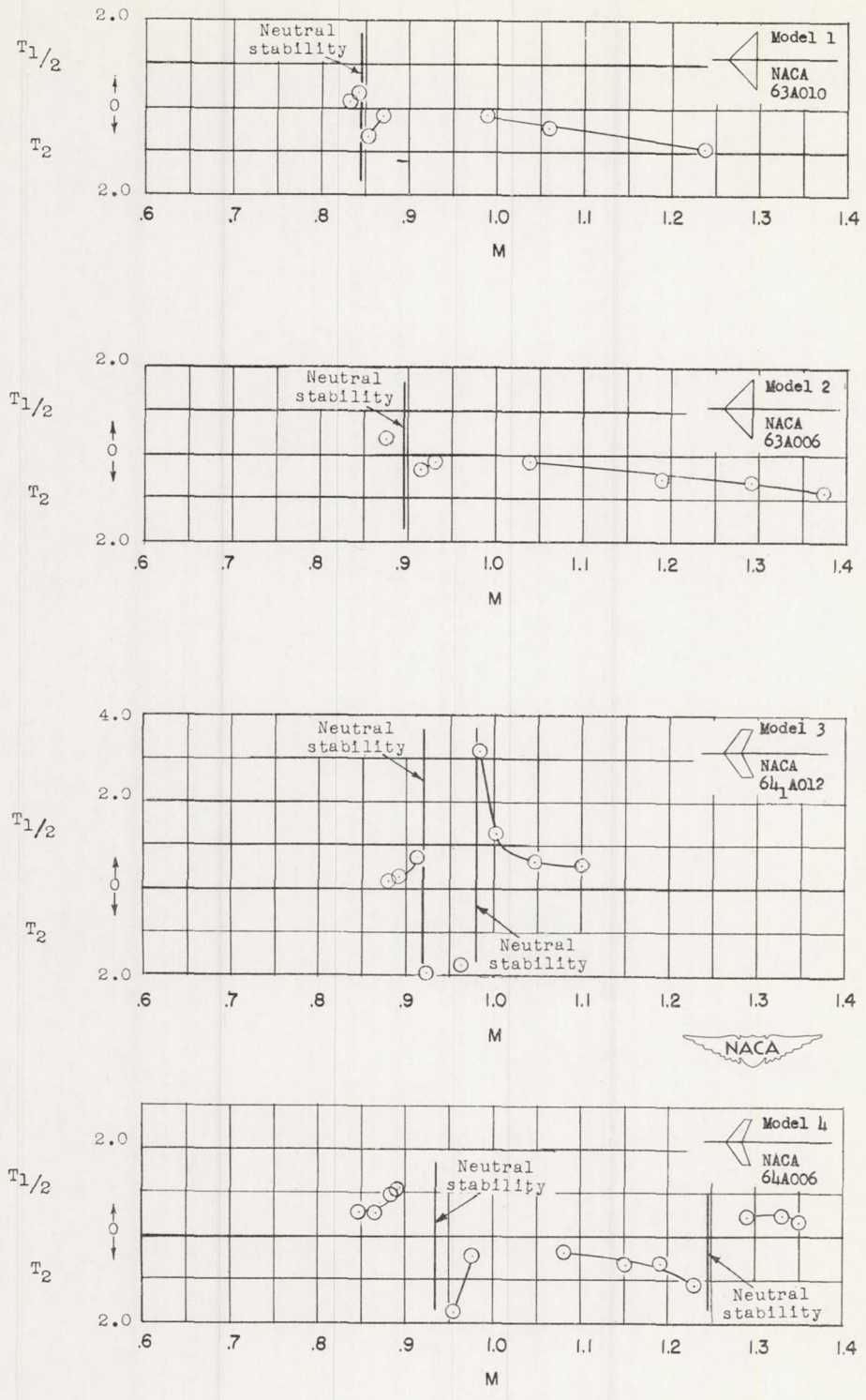

(b) Time to damp.

Figure 8.- Concluded.

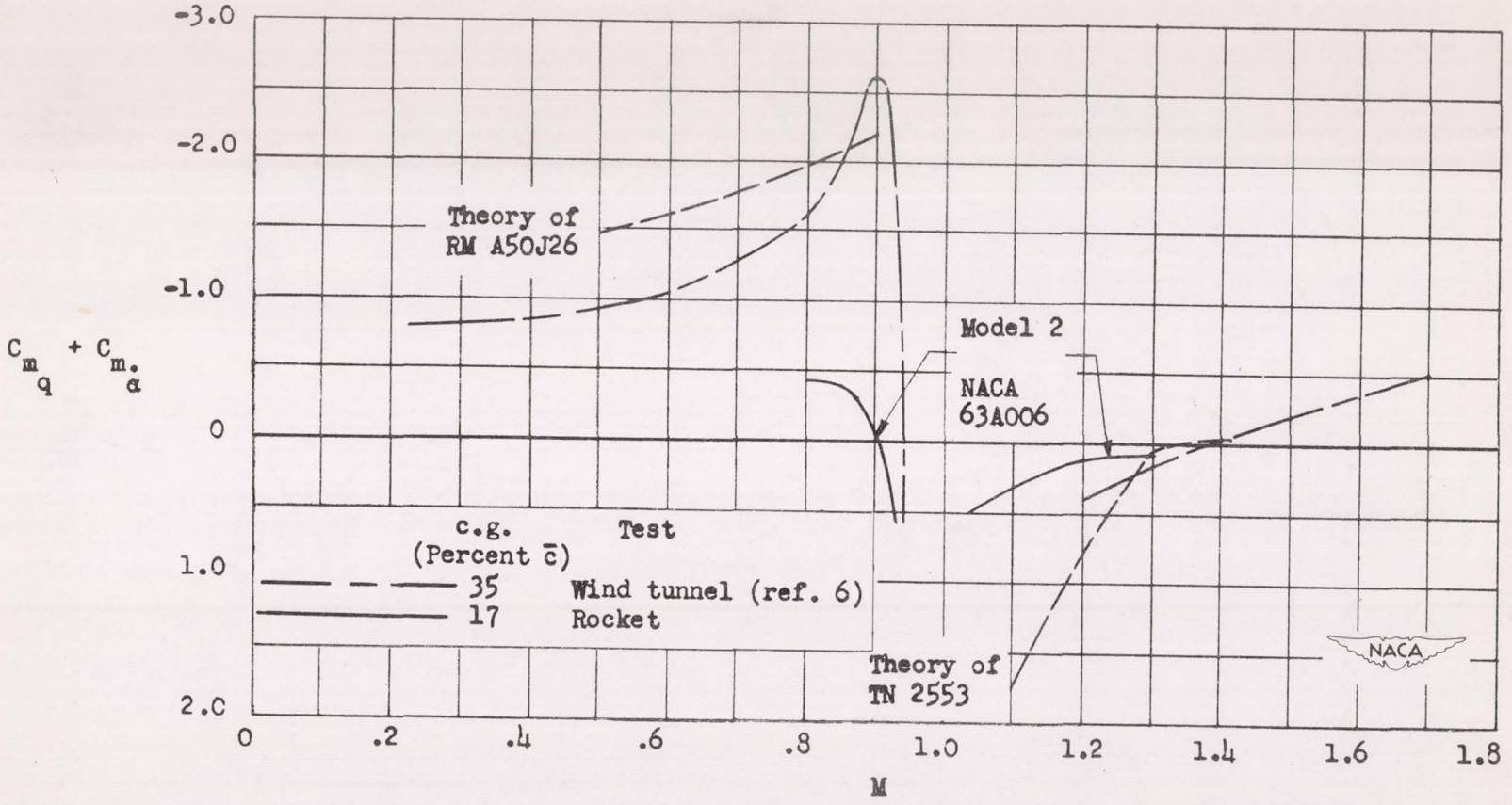

(a) Delta-wing configuration.

Figure 9.- Comparison of rotational damping-in-pitch factor obtained from various tests.

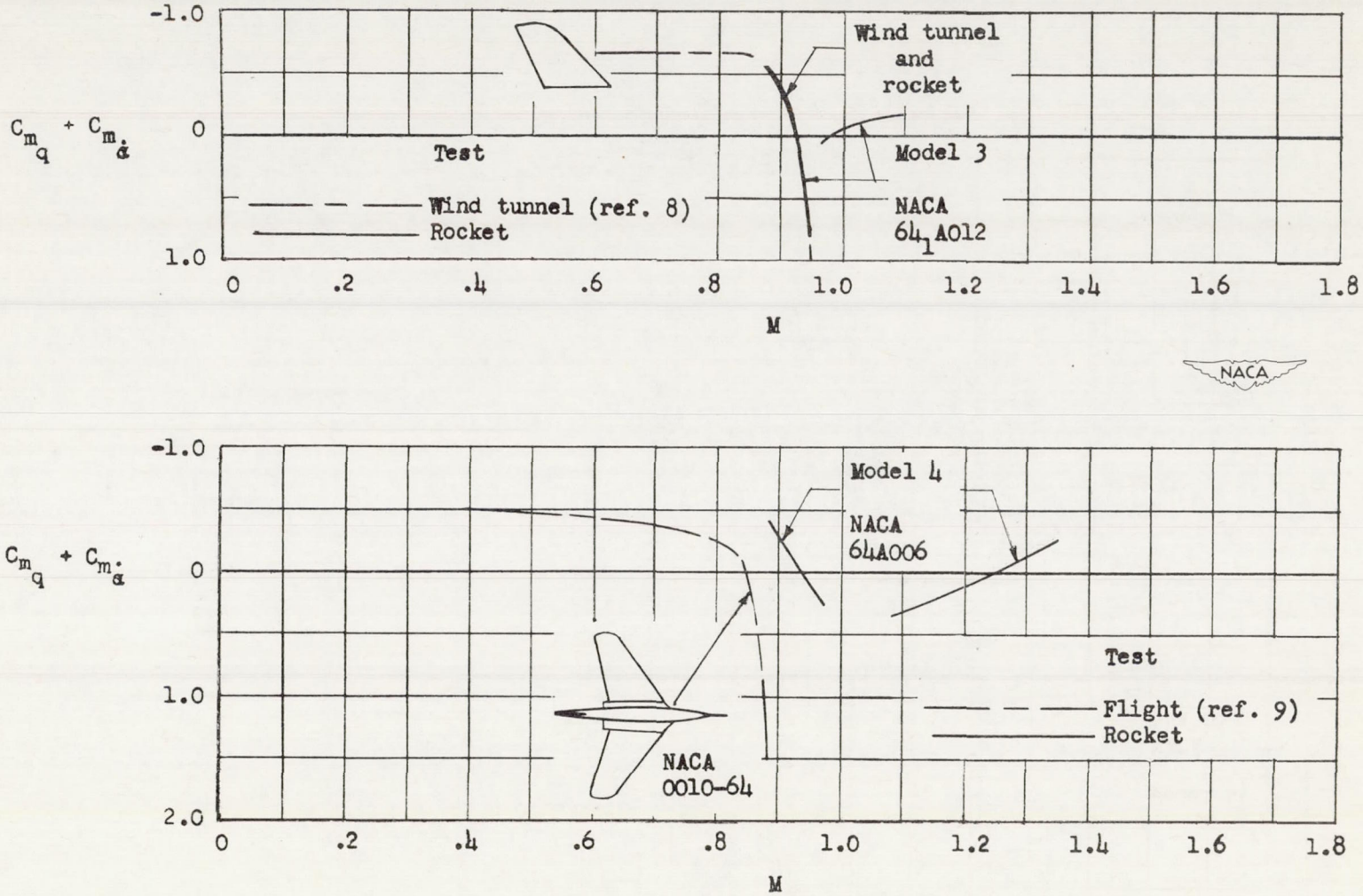

(b) Swept-wing configurations. Center of gravity 17 percent $\bar{c}$.

Figure 9.- Concluded.

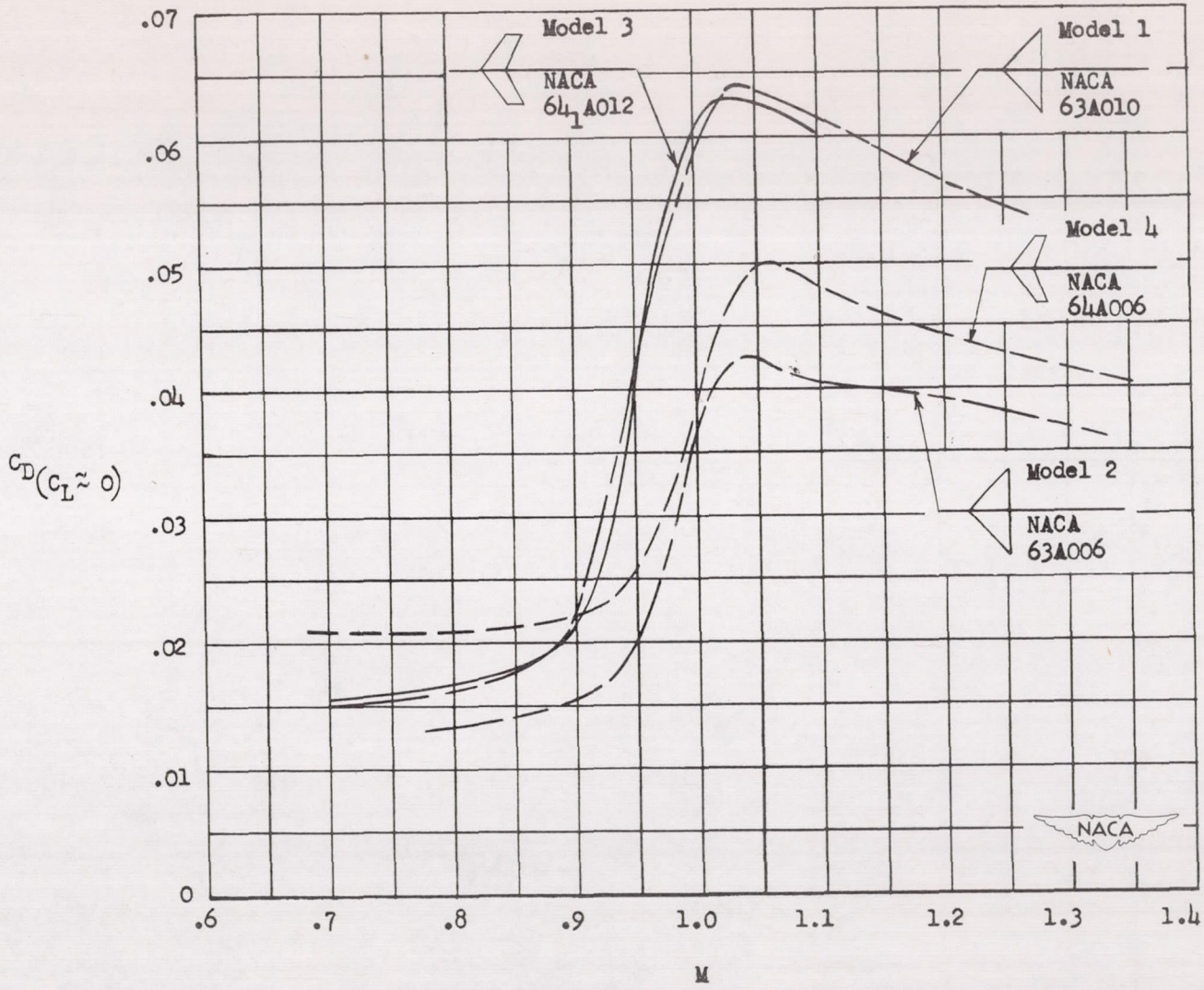

Figure 10.- Variation of drag coefficient near zero lift with Mach number.